Three Dimensional Numerical Simulations of Internal Tides at the Continental Slope and Shelf off Angola

Z. Zeng[1,2], P. Brandt[2,3], K. G. Lamb[4], R. J. Greatbatch[2,3], M. Dengler[2], M. Claus[2,3], and X. Chen[1]

[1] Key Laboratory of Physical Oceanography, Ocean University of China, Qingdao, China

[2] GEOMAR Helmholtz Centre for Ocean Research Kiel, Kiel, Germany

[3] Faculty of Mathematics and Natural Sciences, Kiel University, Kiel, Germany

[4] Department of Applied Mathematics, University of Waterloo, Ontario, Canada

Corresponding author: Zhi Zeng (jtmdawn@foxmail.com)

Key Points:

- Mixing induced by internal tides contribute to the establishment of a cross-shore sea surface temperature gradient on the Angolan shelf
- The impact of internal tide mixing on local environment on the shelf is strongest in austral winter due to seasonally weakest stratification

Abstract

In austral winter, biological productivity at the Angolan shelf reaches its maximum. The alongshore winds, however, reach their seasonal minimum suggesting that processes other than local wind-driven upwelling contribute to near-coastal cooling and nutrient supply, one possibility being mixing induced by internal tides (ITs). Here, we apply a three-dimensional ocean model to simulate the generation, propagation and dissipation of ITs at the Angolan slope and shelf. Model results are validated against moored acoustic Doppler current profiler and other observations. Simulated ITs are mainly generated in regions with a critical/supercritical slope typically between the 200- and 500-m isobaths. Mixing induced by ITs is found to be strongest close to the shore and gradually decreases offshore thereby contributing to the establishment of a cross-shore sea surface temperature gradient. The available seasonal coverage of hydrographic data is used to design sensitivity simulations. Seasonal variations in stratification results in substantial temporal differences in IT characteristics, such as their wavelengths, sea surface convergence patterns and baroclinic structure, additionally showing strong spatial variations. However, seasonal variations in the domain-integrated generation, onshore flux and dissipation of IT energy are weak. By defining a parameter - the relative change of the vertical density gradient - to evaluate the relative mixing strength, it is shown, nevertheless, that mixing due to ITs is more effective at weakening the stratification during austral winter. We argue this is because less energy is required to mix the water column in austral winter than in austral summer.

Plain Language Summary

Tropical eastern boundary upwelling regions (e.g. on the Angolan shelf and Peruvian shelf) usually have high biological productivity. Unlike farther poleward eastern boundary upwelling regions that are forced by trade winds, tropical upwelling regions are characterized by weak winds. Maximum biological productivity of the Angolan shelf is observed in austral winter during periods of weakest winds. Therefore, other factors must contribute to the seasonality in the productivity. Mixing induced by internal tides is one of these possible factors. We have designed numerical simulations to explore the generation, propagation and dissipation of internal tides on the Angolan shelf. It is found that the internal tides on the Angoaln shelf indeed promote the appearance of cold water at the surface near the shore. Furthermore, we explore the seasonal variations of the internal tides taken into account the seasonally varying stratification at the continental slope and shelf. The results show that seasonal variations in the tidal energy available for mixing on the shelf is weak, but less energy is required to mix the weaker stratified waters in austral winter. Therefore, a stronger impact of internal tide mixing on sea surface temperature and biological productivity is suggested to occurr in austral winter.

1 Introduction

Tropical eastern boundary upwelling systems are characterized by rich marine ecosystems [*Carr & Kearns*, 2003]. They undergo strong intraseasonal to interannual variability dominantly associated with equatorial forcing and are often subject to intense hypoxia (e.g., *Mohrholz et al.* [2008], *Bachelery et al.* [2016], *Echevin et al.* [2008]). The Angolan shelf hosts such a tropical eastern boundary upwelling system known for its high biological productivity and fisheries [*Tchipalanga et al.*, 2018]. The main seasonal upwelling is observed during austral winter and is linked to the passage of semi-annual coastally trapped waves forced remotely at the equator [*Rouault*, 2012] and locally by air-sea interaction. However, cold SST anomalies in a small stripe along the coast as observed in satellite data (MODIS, Figure1a) during that period cannot easily be explained. As discussed by *Ostrowski et al.* [2009], the main upwelling season off Angola in austral winter coincides with the seasonal minimum of alongshore winds. While there might be a role for local wind-curl driven upwelling associated with the resulting Ekman divergence, the wind forcing does not appear to be adequate to explain the near-coastal primary productivity maximum during that season. Therefore, *Ostrowski et al.* [2009] hypothesized that other processes such as mixing induced by internal waves may contribute to the near-coastal cooling and upward nutrient supply into the euphotic zone. Moored observations [*Tchipalanga et al.*, 2018] seems to confirm such a hypothesis showing higher internal wave activity near the buoyancy frequency during austral winter compared to austral summer at the continental slope. Nevertheless, it remains to be clarified how internal waves might affect hydrographic characteristics and upward nutrient supply. On the Angolan shelf, shipboard acoustic backscatter images have revealed the existence of tidally generated internal waves propagating from the shelf break toward the coast [*Ostrowski et al.*, 2009]. They found well-developed trains of internal solitary waves (ISWs) during austral winter, while in March (i.e., austral summer) internal waves were more incoherent and generally weaker. Figure 1c shows a synthetic aperture radar (SAR) image from the ERS-1 satellite taken in January (the secondary upwelling season) showing surface signatures of internal waves. The distances between two consecutive trains of ISWs (the white stripes parallel to the shore, marked by red points) that correspond to the wavelength of the internal tides (ITs) are about 23, 21 and 18 km respectively towards the shore.

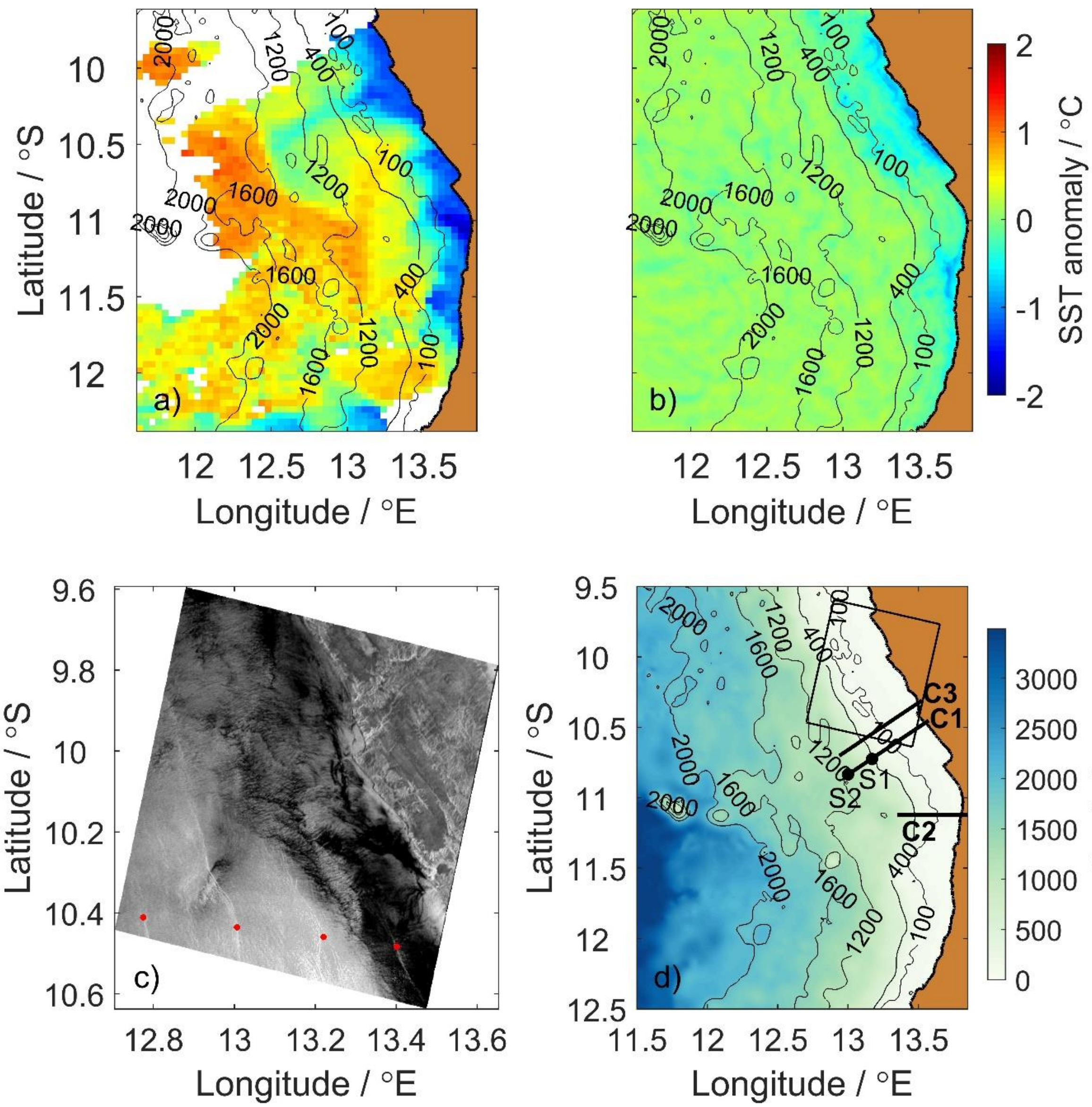

Figure 1. a) SST anomaly observed by MODIS at 21:45 UTC 20 July 2013. b) SST anomaly after 20 M2 tidal cycles of the control simulation. c) ERS-1 SAR image acquired at 0920 UTC 12 Jan 1996; red points indicate internal wave fronts. The contrast of the image has been adjusted. d) Bottom topography used in the control simulation. S1 and S2 are the locations of the two ADCP moorings; C1, C2 and C3 are cross-shore sections; the square marks the location of the SAR image shown in c). Black contours with numbers are isobaths (unit: m).

Stratification on the continental slope/shelf off Angola varies seasonally [*Kopte et al.*, 2017]. These changes are found to be a consequence of 1) semi-annual coastally trapped waves mainly originating in the equatorial Atlantic [*Rouault*, 2012] that are responsible for a main upwelling along the Angolan shelf in austral winter and a secondary upwelling in January and 2) air-sea heat and freshwater fluxes and river run-off responsible for the presence of warm, low-salinity waters at the surface during March/April and November/December [*Kopte et al.*, 2017].

Such changes in stratification on the continental slope/shelf possibly affect the generation and propagation of ITs.

Tidal-frequency internal waves, generated by barotropic tidal flow over topographic obstacles in a stably stratified fluid, lead to local mixing near the generation site, both due to direct wave breaking (close to topography) and enhanced rates of interaction with other internal waves (e.g., *MacKinnon et al.* [2017]). The interaction between low-mode internal tides and large-amplitude topography, such as continental slopes, is strongly dependent on stratification and the steepness of the topography [*Cacchione & Wunsch*, 1974; *Johnston & Merrifield*, 2003; *Legg & Adcroft*, 2003; *Venayagamoorthy & Fringer*, 2006; *Helfrich & Grimshaw*, 2008; *Hall et al.*, 2013; *Legg*, 2014; *Mathur et al.*, 2014]. *Hall et al.* [2013] explored the reflection and transmission of incident low-mode internal tides and found the fraction of energy transmitted to the shore depends, apart from slope criticality, on the strength of stratification on the continental shelf. For a comprehensive review of internal wave generation, propagation and breaking on the continental slope/shelf including several two-dimensional (2D) simulations for a few different topographies please refer to *Lamb* [2014].The main goal of our study is to identify the role of seasonal variations of ITs and associated IT mixing in near-coastal SST variability and, with this, shed some light on the associated variability of biological productivity on the Angolan shelf.

To achieve this, a 3D ocean model that can simulate the generation and propagation of ITs is required. Here we use the Massachusetts Institute of Technology General Circulation Model (MITgcm, see *Marshall et al.* [1997]), which is able to simulate multi-scale processes and has been widely used in many fields of marine research. For example, *Buijsman et al.* [2014] compare 3D and 2D simulations to examine the double-ridge IT interference in Luzon Strait and find IT resonance in 3D simulations is several times stronger. *Mohanty et al.* [2017] adopt in-situ data collected during 19-20 February 2012 to simulate ITs in the western Bay of Bengal and explore their energetic characteristics. *Vlasenko et al.* [2014] also use observational data to conduct simulations and investigate the 3D dynamics of ITs on the continental slope/shelf area of the Celtic Sea. In our study, measured data are used to validate the model and to initialize the temperature/salinity field for the different sensitivity runs. In the control simulation, we simulate the generation and propagation of ITs to explore how they affect velocity and hydrographic fields. In the sensitivity runs, we compare and discuss the results of two seasonal extremes and then focus on the seasonal variation in IT energy and mixing influenced by the seasonal stratification.

2 Data and Methods

2.1 Mooring data

Two moorings S1 and S2 were deployed at the continental slope off Angola (shown in Figure 1d) to measure the velocity from July 2013 to October 2015. Mooring S1, a bottom shield located at 13.20°E, 10.70°S at 500-m depth, corresponding to the steepest part of the continental slope, was equipped with a 75 kHz Teledyne RDI's Workhorse Long Ranger acoustic Doppler current profiler (ADCP) that sampled every 2.5 min. The other mooring (S2) was located at 13.00°E, 10.83°S at 1200-m depth in a region of weak topographic slope and had another upward looking 75 kHz Long Ranger ADCP installed at 500-m depth that sampled every hour. Both ADCPs acquired velocity data up to about 40-m depth below the sea surface.

2.2 Measured temperature and salinity data

The in-situ temperature/salinity data are a combination of shipboard and glider hydrographic measurements [*Tchipalanga et al.*, 2018]. There were 707 shipboard temperature/salinity profiles taken between 11.50°S and 10.00°S, among which 644 profiles were acquired within the EAF-Nansen program between 1991 and 2015. Additionally, 52 profiles were extracted from the input data set for the MIMOC climatology [*Schmidtko et al.*, 2013] and 11 profiles were collected during different R/V Meteor cruises [*Mohrholz et al.*, 2001, 2008, 2014]. To complement the dataset, hydrographic profiles from an autonomous Slocum glider (Teledyne Webb Research, Glider IFM03, deployment-ID: ifm03_depl12) were used, which sampled at around 11.00°S from October to November 2015. The glider acquired 364 temperature/salinity profiles in water depths from 200 to 800 m. These observed temperature/salinity data were interpolated to derive a mean daily climatology with a vertical resolution of 5 m in the upper 500 m below the sea surface. For the sensitivity tests, we averaged the daily data month by month to obtain initial fields for the 12 simulations aimed at studying the seasonal variability.

2.3 Numerical model setup

2.3.1 Control simulation

The MITgcm uses finite volume methods and orthogonal curvilinear coordinates horizontally. The model domain (11.70° - 13.90°E, 9.60° - 12.30°S) that is used for all simulations is shown in Figure 1d. Here we mainly focus on the generation and propagation of ITs. We use a latitude/longitude grid and set the horizontal resolution to roughly 250 × 250 m, which is high enough for the 3D simulations of the ITs in this area, although not sufficient to capture non-hydrostatic effects that are the basis for the generation of ISWs (e.g., *Brandt et al.* [1997], *Apel* [2003]). The MITgcm permits non-uniform vertical spacing and we use an enhanced vertical resolution (5 m) spanning the strongly stratified near-surface layers with coarser resolution (150 m) near the sea bottom. To satisfy the Courant–Friedrichs–Lewy (CFL) condition, the time step is set to 5 s.

Initial conditions are no-flow and horizontally uniform stratification. The temperature and salinity fields (Figures 2a and 2b) are acquired from the observational dataset for July, as described in Section 2.2. The terrain data comes from the GEBCO (General Bathymetric Chart of the Oceans, https://www.gebco.net/data_and_products/historical_data_sets/#gebco_2014) dataset with a high resolution of 1/120°× 1/120°, which is employed after being interpolated to match the grid. The shallowest water depth in the study area is 1 m.

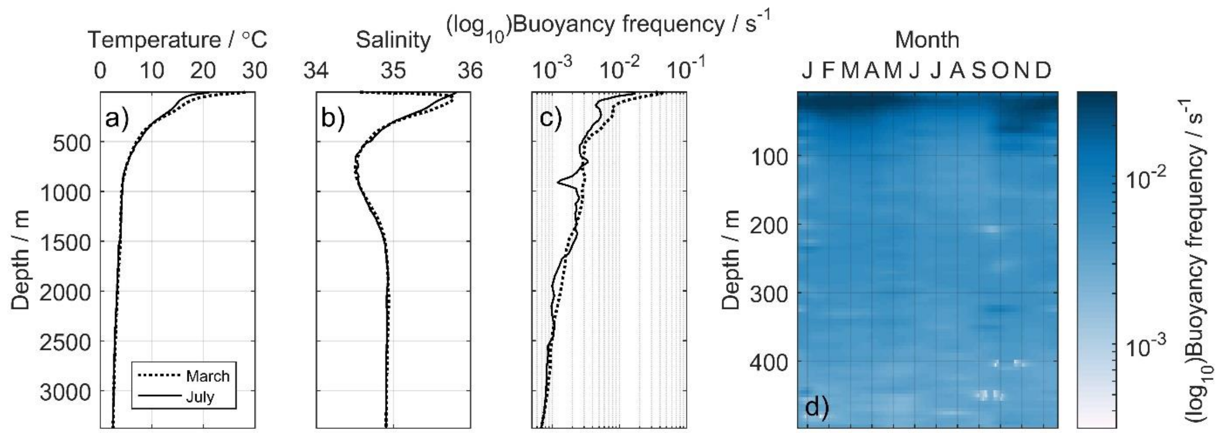

Figure 2. Initial vertical profiles of temperature a), salinity b) and buoyancy frequency c) respectively in the study area. d) Buoyancy frequency in the study area as a function of depth (shallower than 500 m) and months derived from observations.

Boundary conditions are no-slip at the bottom, no-stress at the surface and no buoyancy flux through the surface or the bottom. The simulation is forced by eight tides (K1, O1, P1, Q1, M2, S2, K2 and N2) at open boundaries. The amplitudes and phases of these tides are extracted from the regional solution for Africa provided by the Oregon State University (OSU) inverse barotropic tidal model (OTIS, http://people.oregonstate.edu/~erofeevs/Afr.html) [*Egbert et al.*, 2002]. Furthermore, a sponge boundary treatment with a width of 50 grid points is imposed in which velocity, sea surface elevation, temperature and salinity are damped to the boundary values. Further details about the sponge layers could be referred to *Zhang et al.* [2011]. Note that the “whole domain” in the following refers to the domain excluding the sponge layers and all of our analyses are done in the “whole domain”.

The MITgcm itself provides several vertical turbulence parameterization schemes. The KL10 scheme [*Klymak & Legg*, 2010] is designed to represent mixing in the “interior” ocean. However, it requires a very high resolution and is not recommended for simulating internal tides at the resolution we use. Here, we choose the KPP scheme [*Large et al.*, 1994], which was also successfully applied to the simulation of the generation and propagation of ITs (see examples in Dorostkar et al. [2017], Han & Eden [2019]). For the horizontal mixing scheme, we select the Leith scheme [*Leith*, 1996] as suggested by *Guo & Chen* [2012]. We use the full form of Leith viscosity and provide enough viscous dissipation of vorticity at length-scales smaller than 2 grid cells. The control simulation starts from 00:00 UTC 15 July 2013 and runs to 00:00 UTC 30 July 2013, which includes a spring tide and part of a neap tide. The interval of output data is 1 hour. Model output from the first three days is not included in the following analysis.

2.3.2 Mooring data

To explore the influence of seasonally varying stratification on the IT characteristics, we design 12 sensitivity simulations, corresponding to the 12 months, employing different initial stratification fields derived from observations (Figure 2d). The stratification mainly varies in the upper 500 m. Because of computational and data storage limitations, we set the horizontal resolution to 500 m in these simulations. The reduced resolution was found to be suitable to identify and analyze ITs, which was tested by comparing the results of the control simulation (shown later) and the low-resolution July case. The comparison of the two simulations is shown later. Other parameter settings in the sensitivity simulations are the same as for the control simulation. The same tidal forcing (July case) is used in the 12 simulations to isolate the effect of the changing seasonal stratification on the model results, which allows more straightforward comparisons among the simulations, even though in reality the tides vary during the year.

3 Results

3.1 Model validation

Both simulated and observed velocity at the mooring locations are vertically averaged over the depth range set by the observation limits (S1: 39 to 454 m, S2: 41 to 456 m) and compared over the same period (about 6.5 days) during July 2013 (Figure 3). For location S1, the model results are generally consistent with the observed data, despite some longer-period variations superposed on the tidal currents in the observed data. However, the simulation of cross-shore velocity shows some more significant differences, with the phase of the model velocity being a few hours ahead of that in the observations over the last three days. At station S2, there is a difference in the mean alongshore velocity of around 3.5 cm s^{-1} between model and observations, which likely corresponds to the presence of an alongshore current in the observations associated with the weak poleward Angola Current or intraseasonal and/or seasonal variability [*Kopte et al.*, 2017] that are not related to tidal dynamics. For the cross-shore velocity, the simulated phase also leads that in the observations during the last few days. One possible reason for the differences between model and observations is that the topography (GEBCO) we use might not be accurate enough. For example, the measured water depths at S1 and S2 are 494 and 1227 m while in the simulation they are 441 m and 1184 m, respectively.

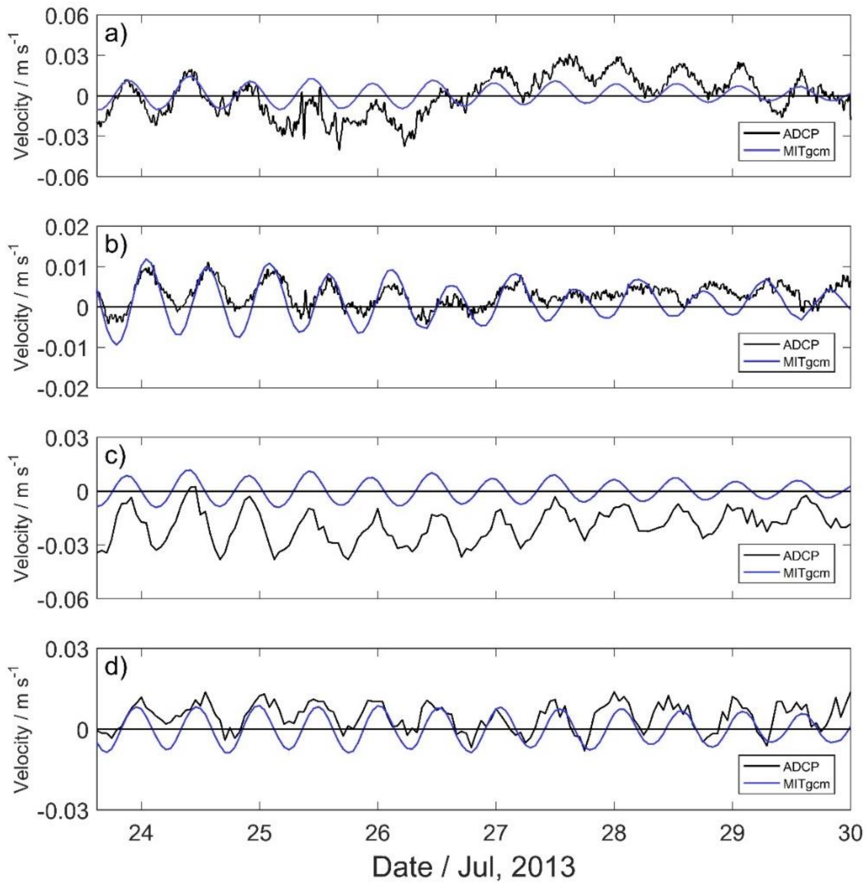

Figure 3. Observed and simulated velocities vertically averaged over 40 - 455 m depth at the mooring positions; alongshore velocity: a) S1 and c) S2; cross-shore velocity: b) S1 and d) S2. Positive alongshore velocity is directed equatorward (north) and positive cross-shore velocity is directed onshore (both rotated by -34° due to the local inclination of the coast).

We conducted harmonic analysis of both the model and measured vertically-averaged velocity of station S1. Due to the limited temporal range in the model (From 18 July to 30 July), only M2 and K1 tidal parameters are acquired (Table 1). The amplitude of M2 and K1 in observations and model agree well, with observed amplitudes being slightly larger.

Table 1 Amplitude of M2 and K1 tidal current velocity at station S1

Tide	Amplitude of velocity / cm s^{-1}			
	M2		K1	
	Alongshore	Cross-shore	Alongshore	Cross-shore
Model	1.29	1.16	0.15	0.19
Observation	1.48	1.39	0.24	0.29

For the comparison over the whole domain, we first contrast the simulated SST anomaly (Figure 1b) with observed values (Figure 1a). The satellite data reveal lower SST near the coast showing some undulations and filaments. In our control simulation, SST is also lower near the coast, though the anomaly is smaller. We then calculate sea surface velocity divergence (SSVD) after 20 M2 tidal cycles of the control simulation to locate the IT fronts [*Zhang et al.,* 2011]. In the north square at around 10.50°S (Figure 4a), the distance between two consecutive wave fronts is about 10 km decreasing toward the coast (this can be more clearly seen in Figure 5a discussed below), which is about half that in the SAR image. This is because the IT wavelength has a seasonality due to different seasonal stratification on the shelf (see Figures 6a and 6b). The wavelength in March is about twice in July. The SAR image (Figure 1c) is taken in January and the observed wavelengths are more consistent with the results of our March case (see Figures 6b and 7b).

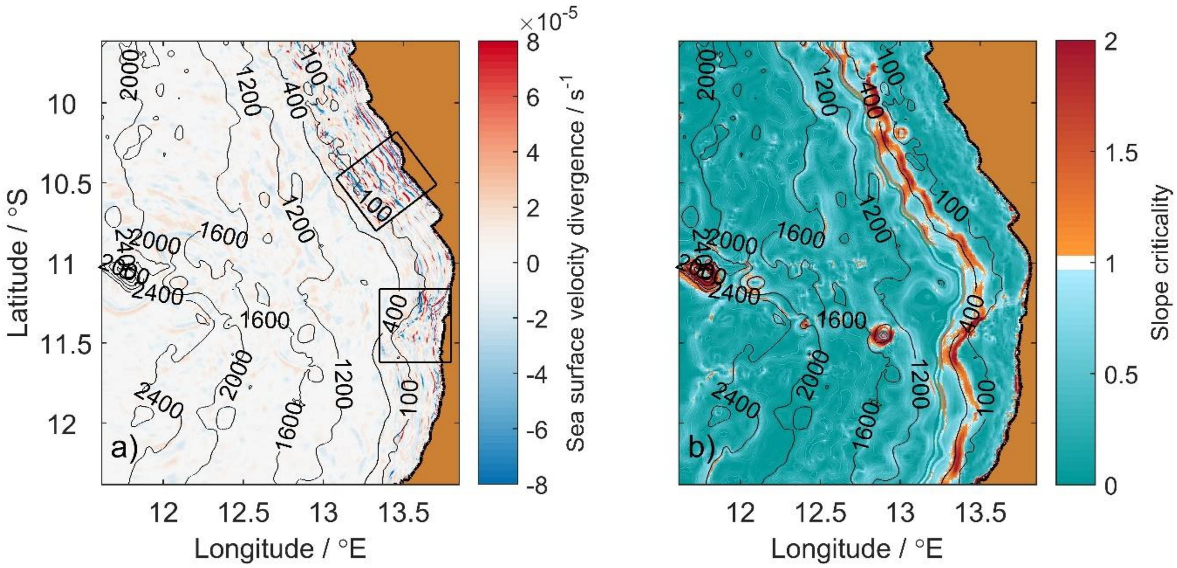

Figure 4. a) Sea surface velocity divergence after 20 M2 tidal cycles of the control simulation; b) slope criticality for M2 tide of the control simulation. Black contours with numbers are isobaths (unit: m).

3.2 Generation and propagation of internal tides

In a first step, we calculate the slope criticality α to identify the generation sites. α is the ratio of the topographic slope to the internal wave characteristic slope, which can be used to predict the behavior of incident waves approaching a topographic slope from offshore [*Gilbert & Garrett* 1989; *Nash et al.*, 2004]:

$$\alpha = \frac{S_{topo}}{S_{wave}} = \frac{\partial H / \partial x}{\left[\left(\omega^2 - f^2\right)/\left(N^2 - \omega^2\right)\right]^{1/2}}, \tag{1}$$

where H is the water depth, x the cross-slope distance, ω the angular frequency of the wave, f the inertial frequency and N the buoyancy frequency. $\alpha < 1$, $\alpha = 1$ and $\alpha > 1$ respectively means subcritical, critical and supercritical topography. Incident waves are transmitted upslope into waves with shorter wavelength if $\alpha < 1$ while partially reflected back toward deeper water if $\alpha > 1$ [*Lamb*, 2014]. Nonlinear and/or viscous effects are enhanced when $\alpha = 1$ [*Dauxois et al.*, 2004]. When barotropic tides propagate over a near-critical or supercritical slope, internal wave/tidal beams are produced due to the interactions between tides and topography [*Shaw et al.*, 2009] and the conversion from barotropic energy to baroclinic energy is especially effective. In our simulations forced by barotropic tides, one may expect barotropic tides transfer energy to ITs when propagating over near-critical or supercritical regions in the study area. As the hydrostatic approximation is adopted in our simulations, the term $\left(N^2 - \omega^2\right)$ in (1) is replaced by N^2. We use N^2 from the horizontally-homogeneous initial field at local water depth and the M2 tidal period to derive the distribution of α (Figure 4b). The result shows the main critical and supercritical regions are between 200- and 500-m depth along the continental slope. In Figure 4a, the ITs are mainly distributed on the shelf shallower than 400 m and the wave fronts are generally parallel to the isobaths. Therefore, it is suggested that the generation sites of the ITs are located along the isobaths of around 400 m.

By comparing the SST anomaly in Figure 1b with the SSVD in Figure 4a, it is evident that regions with higher SST anomaly correspond to regions with enhanced SSVD signals, see the two squares in Figure 4a. This implies the ITs locally cause mixing that results in sea surface cooling. The climatological stratification of the Angolan shelf we use is formed by all processes that can change the stratification, including IT mixing. Therefore, we select several cross-shore sections as indicated in Figure 1d to focus on emerging horizontal gradients as well as to explore the local variations of dynamic and hydrographic properties.

Figure 5a shows the baroclinic velocity as well as isotherms after 20 M2 tidal cycles along section C1 of the control simulation. Four locations with relatively high horizontal baroclinic velocity formed by the onshore propagating ITs are indicated by inverted triangles in Figure 5a. At these locations, the direction of baroclinic velocity near the sea surface and bottom is opposite to that in the mid layers. Consistently, the isotherms bend between the upper and the mid layers and between the mid and deeper layers, giving the impression of predominantly second baroclinic mode waves. The distances between two consecutive inverted triangles are 11.2, 9.7 and 7.2 km as they shoal from water depths of 112 to 44 m.

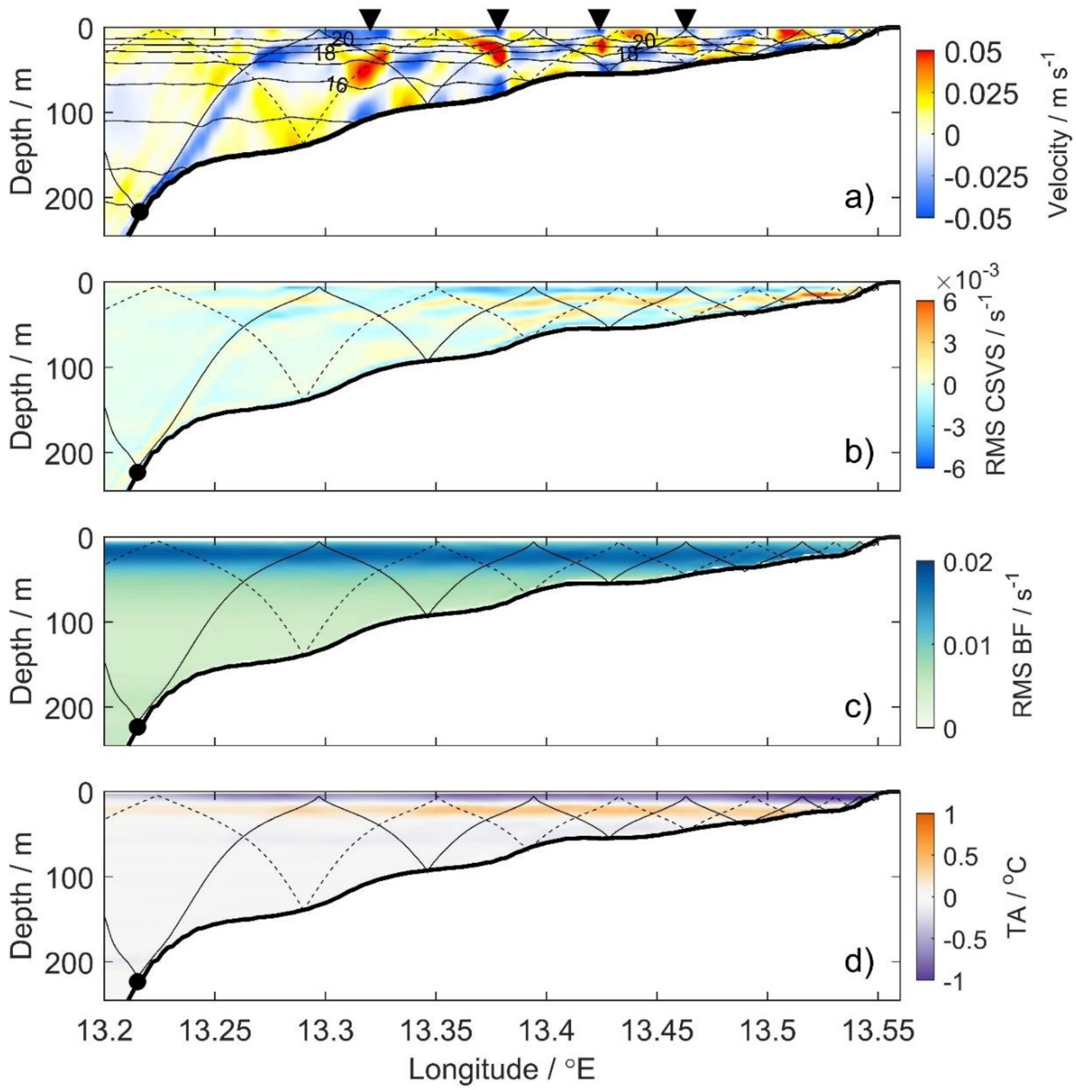

Figure 5. a) Cross-shore baroclinic velocity and d) temperature anomaly (TA) along section C1 after 20 M2 tidal cycles of the control simulation; contoured lines with numbers in a) are isotherms (unit: °C). b) RMS cross-shore velocity shear (CSVS) and c) RMS buoyancy frequency (BF) calculated over last 2 M2 tidal cycles. Overlaid black solid lines originating at the critical point (black dot) are primary M2 tidal beams allowing reflections at the surface and at the bottom. The dashed lines are secondary M2 tidal beams starting at another generation point further offshore. The inverted triangles indicating the location of high baroclinic velocity are discussed in the text.

Next, we note that the topography is subcritical above the critical point ($\alpha = 1$) at 13.22°E (black dot in Figure 5a) and supercritical below that point. We calculate M2 tidal beams emanating from this point (solid lines in Figure 5a emerging from the critical point) and allow reflection at sea surface and bottom. Note that the stratification used in the calculation is temporally averaged over the last 2 M2 tidal cycles, thus the stratification varies horizontally. Baroclinic velocity is enhanced along the upward beam emitting from the critical point, which suggests that when the barotropic tide arrives in the vicinity of the critical point, barotropic energy is converted into baroclinic energy effectively, resulting in the generation of ITs. Apart from the primary beam, we notice a secondary beam (dashed lines in Figure 5a) that comes from a farther offshore generation site. Along this beam the baroclinic velocity is also strengthened. As the ITs propagate onshore, vertical shear of horizontal velocity appears. The RMS cross-shore vertical velocity shear over the last 2 M2 tidal cycles (note that the following parameters referring to "RMS" are all temporally averaged over the last 2 M2 tidal cycles of the different simulations) is shown in Figure 5b. Higher values occur near the coast, which suggests stronger vertical mixing as the applied KPP scheme includes a contribution based on the gradient Richardson number [*Large et al.*, 1994]. Due to the enhanced mixing, stratification becomes weaker and the pycnocline broadens (Figure 5c). In the initial profile of the buoyancy frequency, the maximum value appears at 22.5 m depth. At that depth, the RMS buoyancy frequency is reduced to 1.51×10^{-2} s^{-1} at 13.53°E (water depth 24 m) while it remains 1.84×10^{-2} s^{-1} at 13.20°E (water depth 289 m). Consequences of mixing are also seen from the change of temperature/density. Figure 5d shows the temperature anomaly after 20 M2 tidal cycles relative to its initial value. Water becomes colder near the sea surface (about 0 - 20 m depth depending on the location) while it becomes warmer below (about 25 - 45 m depth). The near-surface cooling is enhanced closer to the coast where SST decrease by more than 1°C. The variation of density is in accordance with temperature changes (not shown) - the density increases near the surface and decreases in deeper layers.

3.3 Seasonal variability of internal tides

The spatially averaged stratification varies significantly from austral winter (JAS) to austral summer (FMA) (Figure 2d). During austral winter, the pycnocline is weak and shallow. The maximal buoyancy frequency is less than 1.8×10^{-2} s^{-1}. The strongest stratification is present during March (austral summer) when the buoyancy frequency can reach 3.4×10^{-2} s^{-1}. The depth of the pycnocline is located between 10- and 60-m depth throughout the year. According to this seasonal variation of stratification that was inferred from observations, March and July are two extreme months. Therefore, we select these two months as exemplar cases to compare their results.

Before comparing the two extreme cases, it is necessary to validate our choice of a reduced horizontal resolution for the sensitivity simulations by comparing the results of the control simulation with the July case. The only difference between them is the horizontal resolution (see Section 2c). The spatial distributions of the SSVD are very similar by comparing Figures 4a and 6a. The two regions with enhanced SSVD in Figure 6a (marked by two squares) are similarly located at around 10.60°S and 11.30°S near the coast. The main difference is that the amplitude of the SSVD is larger in the control simulation, which is a direct consequence of its higher resolution (due to better resolved internal waves, bathymetry and less numerical dissipation). We conclude, also by comparing Figure 5 with the left column of Figure 7, that the resolution reduction does not significantly change the results and, in particularly, it does not affect the comparisons among different sensitivity simulations.

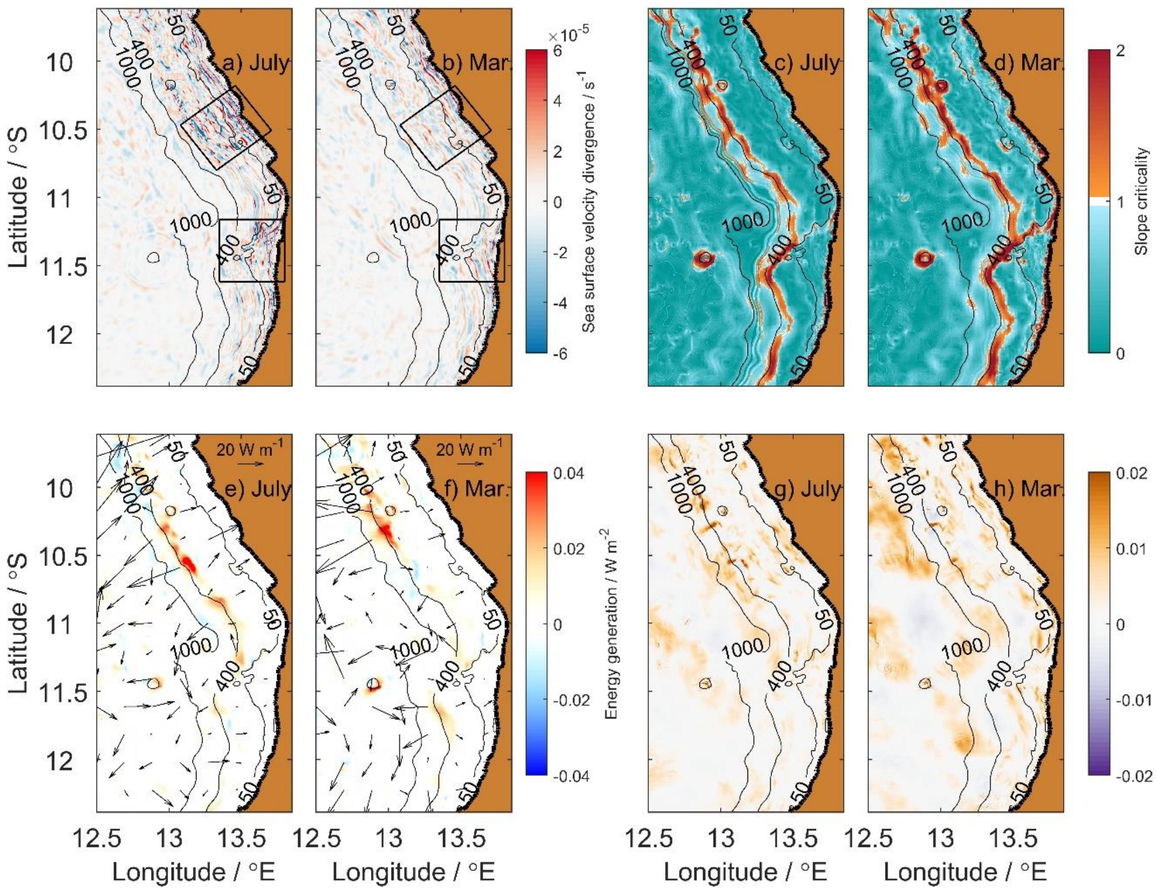

Figure 6. a) - b) SSVD after 20 M2 tidal cycles; c) - d) slope criticality; e) - f) energy generation (contoured) and energy flux (black arrows) of the eight tides; g) - h) energy dissipation of the eight tides. Black contours with numbers are isobaths (unit: m).

Coming back to the two extreme cases of March and July, we first consider the distribution of α that is related to the generation of the ITs (Figures 6c and 6d). The main generation site is along the 400-m isobath at the continental slope in March as well as in July. However, in March the supercritical region is slightly enlarged. Additionally, some small supercritical regions in water depths shallower than 100 m appear that are not present in July. For the deep basin, the distribution of α of the two months appear to be very similar, which is due to the vertical distribution of buoyancy frequency in deep layers differing little between the two months. Overall, the difference in slope criticality is small throughout the year, which is also seen from the spatially averaged value (see below). Next, we focus on the propagation characteristics of the ITs. The two regions of enhanced SSVD in March (Figure 6b, marked by two squares) differ from those in July (Figure 6a). Both of them are limited to shallower depths (shallower than 50 m) and the northern one is 0.5° farther north (around 10.10°S) while the southern one shifts 0.2° southward (around 11.50°S). Overall, the SSVD signals are stronger in July. Then we select a typical snapshot of baroclinic velocity along section C1 (Figures 7a and 7b). To focus on near-surface variability, velocity and isotherms are only shown in the upper 150 m. The wavelengths of ITs are substantially larger in March due to the stronger stratification, which can be seen by the larger distances between two consecutive locations of high baroclinic velocity (marked by two inverted triangles in Figure 7b). Compared to July, in March the amplitudes of baroclinic velocities and isotherm displacements are smaller. The vertical structure of the baroclinic current in March differs from that in July, as it changes direction with depth more than twice from the surface to bottom with the isotherms also correspondingly changing curvature. This suggests a dominance of higher baroclinic modes in March forming a well-developed IT beam reflecting at the surface and at the bottom, while in July second baroclinic mode waves dominate on the shelf. Moreover, the occurrence of M2 tidal beams is also different. The second beam is much weaker in March and hard to identify in the vertical distribution of baroclinic current while in July two beams can be clearly identified. To compare a more integral parameter, we calculate the RMS vertical shear of the baroclinic velocities along section C1 (Figures 7c and 7d). It is stronger in July on the shelf. In accordance with the chosen KPP mixing scheme, the enhanced velocity shear and reduced stratification results in stronger mixing in July, thus having larger impact on the initial hydrographic fields. The buoyancy frequency reaches its maximum at 22.5 m depth in the initial profile in both March and July. At that depth, the maximum of RMS buoyancy frequency at 13.55°E (water depth 23 m) decreases to 1.53×10^{-2} s^{-1} in July and 3.2×10^{-2} s^{-1} in March, corresponding to a decrease of 16 % and 6 % relative to the initial values, respectively. Also compared to the initial values, temperature near the surface decreases by up to 0.96°C in July and 0.87°C in March (Figures 7g and 7h); density near the surface increases by up to 0.30 kg m^{-3} in July and 0.24 kg m^{-3} in March (not shown).

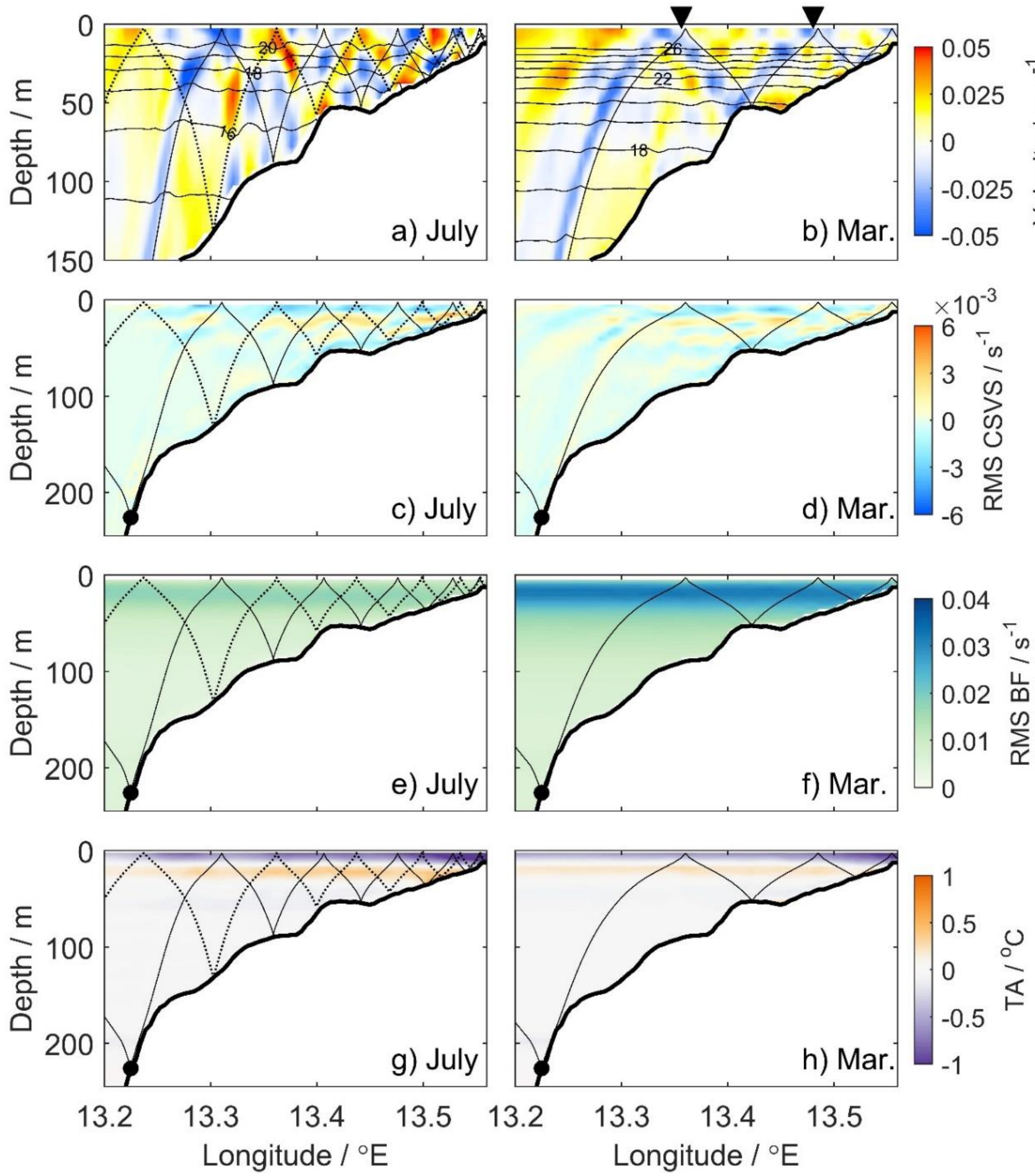

Figure 7. a) - b) Cross-shore baroclinic velocity and g) - h) temperature anomaly (TA) along section C1 after 20 M2 tidal cycles; contoured lines with numbers in are isotherms (unit: °C). c) – d) RMS cross-shore velocity shear (CSVS) and e) - f) RMS buoyancy frequency (BF) calculated over last 2 M2 tidal cycles. Overlaid solid and dashed lines are different M2 tidal beams. The inverted triangles indicating the location of high baroclinic velocity are discussed in the text.

3.4 Internal tide energetics

Now we focus on the generation and propagation of IT energy. As mentioned above, the supercritical region in the study area is slightly larger in March than in July. This is somewhat contradictory to the result that ITs are weaker in March. To address this question, we calculate several parameters of the IT energy budget for these two cases. At each grid point, the conversion rate from barotropic to baroclinic tides (hereafter called "energy generation") C for a specific tidal frequency θ is [*Niwa & Hibiya*, 2004; *Buijsman et al.*, 2012, 2014]:

$$C = \frac{1}{T_\theta} \int_0^{T_\theta} p'_\theta(-H,t)\, w_{bt\theta}(-H,t)\, dt\ , \tag{2}$$

where $p'_\theta(-H,t)$ is the pressure perturbation at the bottom, -H, and $w_{bt\theta}$ the vertical component of barotropic tidal flow. T_θ is usually a multiple of the tidal period and here we choose 10 M2 tidal cycles around spring tide. The pressure perturbation (also called the baroclinic perturbation) is the instantaneous pressure $p_\theta(z,t)$ minus the temporally-averaged pressure $\overline{p_\theta}(z)$ and the temporally varying pressure $\overline{p_0}(t)$:

$$p'_\theta(z,t) = p_\theta(z,t) - \overline{p_\theta}(z) - \overline{p_0}(t). \tag{3}$$

The $\overline{p_0}(t)$ can be calculated through the baroclinicity condition:

$$\overline{p_0}(t) = \frac{1}{H+\eta} \int_{-H}^{\eta} \left[p_\theta(z,t) - \overline{p_\theta}(z) \right] dz\ , \tag{4}$$

where η is the instantaneous sea surface elevation. The bottom boundary condition is

$$w_{bt\theta}(-H,t) = \mathbf{u}_{bt\theta} \cdot \nabla(-H), \tag{5}$$

where $\mathbf{u}_{bt\theta}$ is the horizontal barotropic velocity vector. The vertical-integrated baroclinic energy flux $\mathbf{F}$ represents the IT energy flux away from the generation site and is given by:

$$\mathbf{F} = \frac{1}{T_\theta} \int_0^{T_\theta} \int_{-H}^{\eta} \mathbf{u}'_\theta(z,t)\, p'_\theta(z,t)\, dz dt\ , \tag{6}$$

where $\mathbf{u}'_\theta(z,t)$ is the horizontal velocity perturbation (i.e., the baroclinic velocity perturbation) calculated as the instantaneous horizontal velocity $\mathbf{u}(z,t)$ minus the temporally-averaged velocity $\overline{\mathbf{u}_\theta}(z)$ and the temporary varying barotropic velocity (vertically-averaged velocity) $\overline{\mathbf{u}_0}(t)$:

$$\mathbf{u}'_\theta(z,t) = \mathbf{u}(z,t) - \overline{\mathbf{u}_\theta}(z) - \overline{\mathbf{u}_0}(t). \tag{7}$$

Figures 6e and 6f show the spatial distributions of energy generation and vertically-integrated energy flux. High energy generation is mainly found along the 400-m isobath, both for July and March. However, there are spatial differences. Although the area of high energy generation at around 10.35°S in March is more extended than the one at about 10.55°S in July, most of the energy generated there in March propagates offshore rather than onshore (see the arrows in Figure 6f). By contrast, the percentage of the energy propagating onshore is higher in July. That might explain why there are stronger SSVD signals at about 10.60°S (the northern square in Figure 6a) in July than in March. Nevertheless, there is not always a correspondence between enhanced energy flux and SSVD signals. For example, a large part of IT energy at around 10.44°S propagates offshore in March (Figure 6f) but there is no obvious SSVD in this region (Figure 6b). One likely reason is smaller wave amplitudes and longer wavelengths which results in lower SSVD fields at greater depth compared to those on the shelf.

Next we calculate the energy dissipation. In steady state with ITs comprised of nearly sinusoidal waves, the energy budget can be written as [*Nash et al.*, 2005; *Kelly & Nash*, 2010]:

$$C - \nabla \cdot \mathbf{F} = D, \tag{8}$$

where D represents all processes removing energy from the ITs [*Alford et al.*, 2015] including dissipation and transfer of energy to higher-frequency waves. In our simulations, energy transferred to small scales by nonlinearity is dissipated rather than balanced by dispersion due to the coarse resolution, and D approximately represents local dissipation of IT energy. We calculate D for the two cases (Figures 6g and 6h) and find that the distribution shows high spatial variability. In July relatively high values are distributed at around 10.60°S near the generation sites while in March it is more concentrated at about 10.40°S in depths greater than 1000 m.

We now consider seasonal variations of IT energy. The vertically-integrated energy flux along section C1 is calculated as a function of the months (Figure 8a) and the supercritical points ($\alpha > 1$) are marked for each month (black dots). Generally, one may expect that IT energy is generated near the critical/supercritical region and propagate away in two opposite directions. However, except for June and July, the energy flux is towards the coast in the area whose water depth is deeper than 400 m (the generation sites). This behavior is quite unusual regarding the whole domain (Figure 6e and 6f). Therefore, we select two other cross-shore sections C2 and C3 (see Figure 1d; C3 is parallel to C1 and 10 km north of C1) to compare the results (Figures 8b and 8c). The seasonal cycle of energy flux differs quite substantially from section to section. The main feature at section C2 and C3 is a flux divergence that is strongest at the shelf break but they show distinctly different seasonal cycles: for section C2 maximum flux divergence at the shelf break is in February/March and October/November; for section C3 the maximum occurs in June-September. These differences indicate high spatial variability in the seasonal IT energy flux distribution. What is common to all sections is an onshore IT energy flux on the shelf shallower than 200 m. Here some differences emerge due to the presence of additional supercritical regions on the shelf during parts of the year.

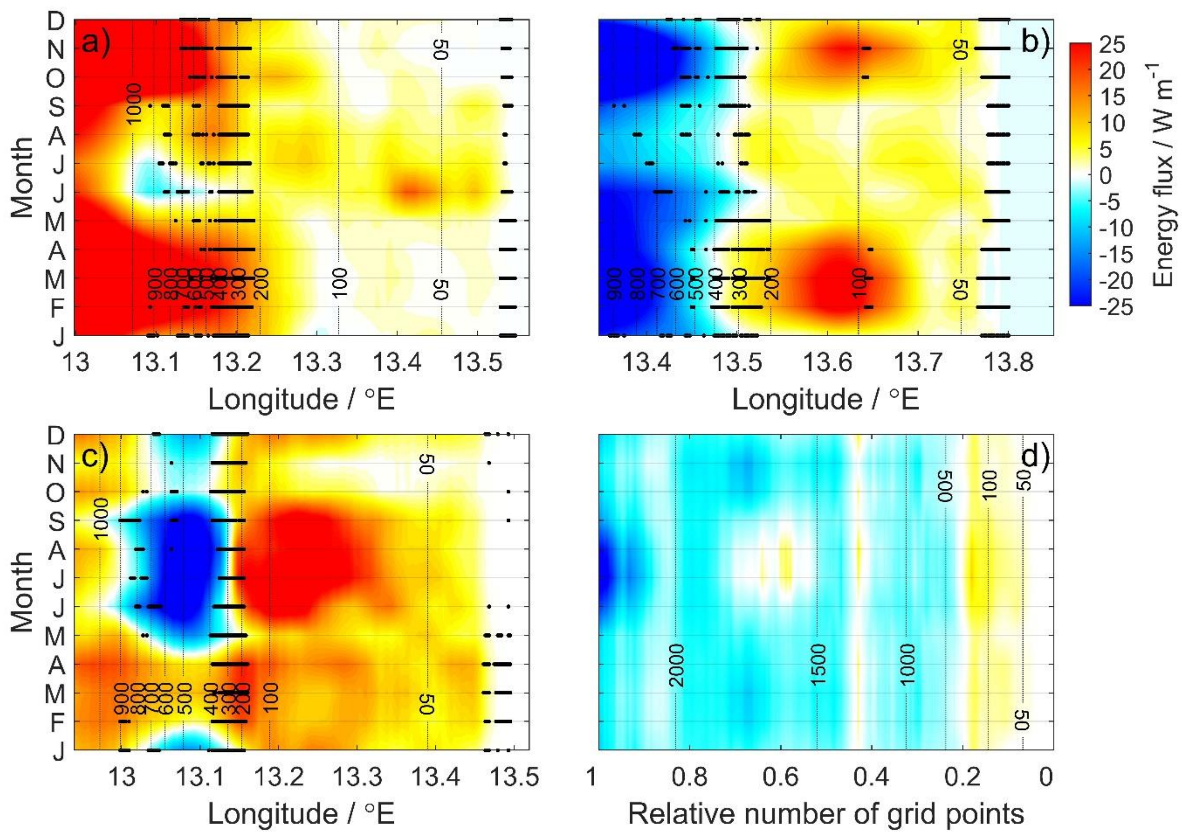

Figure 8. Seasonal vertically-integrated onshore energy flux along section a) C1, b) C2 and c) C3; black dots are supercritical points along the sections. Positive values mean onshore direction. d) Seasonal spatially-averaged vertically-integrated onshore energy flux as a function of relative number of grid points. Black dashed lines with numbers are isobaths (unit: m).

Next, we calculate the onshore energy flux for the whole domain. For every grid point we determine the shortest distance to the coast. The corresponding direction is regarded as the onshore direction. If there is the same shortest distance to different grid points at the coast, we use the average direction. Meanwhile, we classify each grid point in the whole domain according to its water depth and divide the number of grid points shallower than a certain depth by the total number of grid points (not including land grid points). In this way, the relative number of grid points is 0 at the coast and 1 at the deepest grid point. Then we average the onshore energy flux of different grid points for fixed depths and make it a function of months and the relative number of grid points (Figure 8d, note that the right side corresponds to the coast). Although the flux has a strong seasonal variability for a certain cross-shore section, the spatially-averaged flux over the whole domain changes only weakly throughout the year. The energy flux is close to zero along the 400-m isobath where the topography is critical/supercritical (see Figure 9c). It is positive shallower than the supercritical regions and negative in deeper regions. This pattern of energy flux confirms the generation sites of the ITs. Between 1500 and 2000 m there is some onshore energy flux during austral winter, but this is not further explored in this paper.

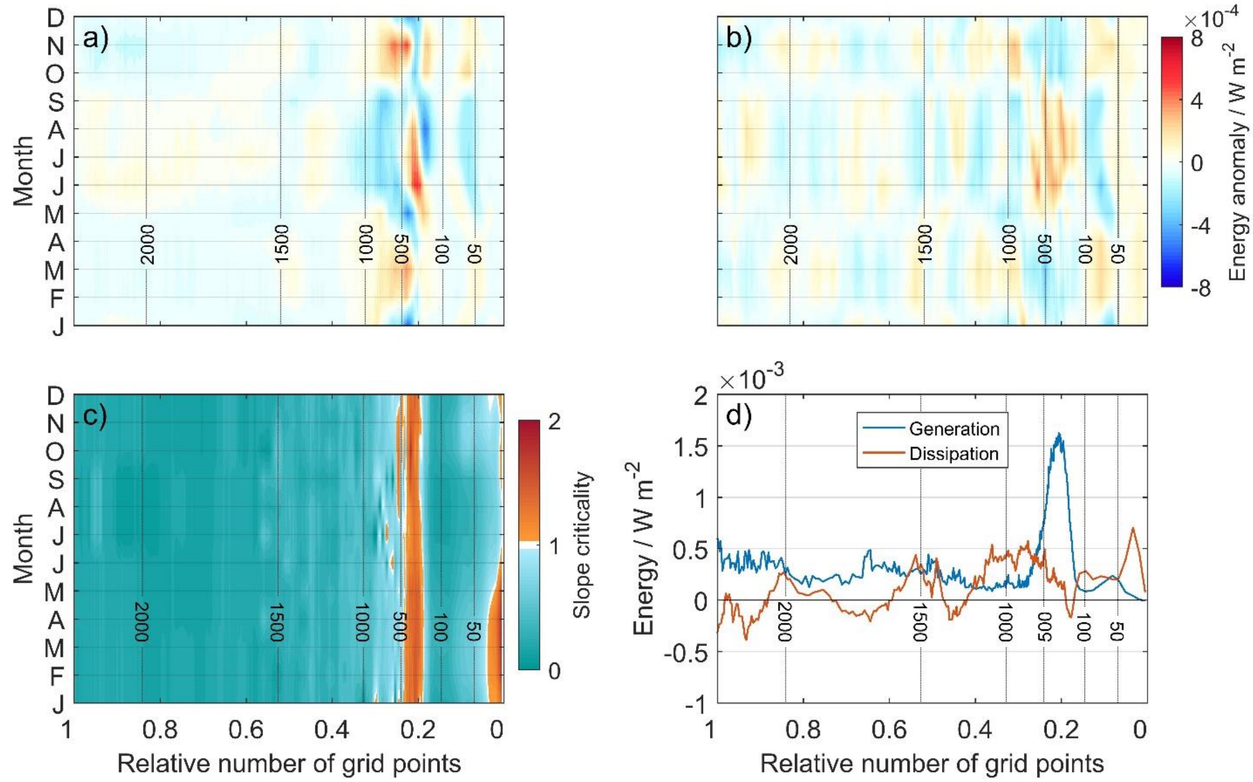

Figure 9. Seasonal anomaly of the spatially-averaged IT energy a) generation and b) dissipation. c) Seasonal spatially-averaged slope criticality. d) Temporally-averaged IT energy generation and dissipation over the whole year. Black dashed lines with numbers are isobaths (unit: m).

Similarly, we also calculate the seasonal energy generation anomaly (relative to the temporally-averaged value over the whole year), dissipation anomaly and slope criticality as functions of the relative number of the grid points (Figures 9a-c). The temporally-averaged values are shown in Figure 9d. IT energy generation mostly occurs in water depths between 200 and 500 m for all months and its seasonal variability mainly appears shallower than 1000-m depth. Both the maximum and minimum values appear in austral winter but total energy generation between 100 - 1000 m does not vary significantly over the year, although the distribution has a spatial variability. During austral winter, the depth range of enhanced values of generation (larger than 6×10^{4} W m^{-2}) is narrower (around 300 to 500 m), which suggests that IT energy generation is more spatially-concentrated. For the whole domain, the seasonal variations of IT energy generation is small compared to the temporally averaged values (cf. Figures 9a and 9d).

Energy dissipation does not show a particular focus area, but is distributed more evenly over different depth ranges (Figure 9b). The highest temporally averaged value appears between 0 and 50 m (Figure 9d), a region that shows particularly weak seasonality. A strong seasonal cycle of dissipation is found for areas with water depths between 50 and 100 m as well as between 100 and 1000 m. While in the shallower depth range maximum dissipation is found during February/March and October/November, for the deeper depth range maximum dissipation appears during June-August.

4 Discussions and conclusions

Tidally generated internal waves play an important role in providing energy for turbulent mixing in the ocean [*Munk & Wunsch,* 1998]. On the Angolan shelf, mixing processes related to ITs are thought to represent a vital controlling factor for biological productivity [*Ostrowski et al.*, 2009] and water mass properties [*Tchipalanga et al.*, 2018]. The results of our control simulation are used to study the generation of IT, its onshore propagation and its impact on mixing and water mass properties. The main generation sites of ITs on the shelf are along the continental slope between the isobaths of 200 and 500 m. The IT fronts are nearly parallel to the shore/isobaths. During austral winter, the distance between two consecutive fronts is about 10 km along section C1 and the ITs are mainly in the form of second mode waves (Figure 5a) seen from the vertical structure of baroclinic current along with isotherm displacement. Enhanced baroclinic velocities along tidal beams suggests the appearance of ITs on the shelf are the results of the interaction of the barotropic tide with critical/supercritical topography [*Lamb*, 2014]. Beside the primary M2 IT beam originating at the upper critical point of the main supercritical region at the continental slope, a secondary M2 tidal beam is identified (Figure 5a) originating farther offshore. It modulates the vertical structure of the baroclinic current on the shelf and likely contributes to the formation of the second-mode ITs. As the ITs propagate onshore, the cross-shore velocity shear increases (Figure 5b) while stratification on the shelf weakens. Consistently, the temperature/density is decreased/increased in a near-surface layer and increased/decreased beneath it with the temperature/density anomalies increasing toward the coast. Note that if there were no tidal forcing, the near-coastal regions would actually become warmer over time due to spatially uniform vertical mixing of the homogeneous initial temperature profile [*Davidson et al.*, 1998]. The cooling of SST near the coast in our simulation is thus a consequence of the tidal forcing. In this case, the change of the physical properties along section C1 suggests that enhanced IT mixing on the shelf contributes to the establishment of near-coastal cross-shore SST gradients corresponding to the satellite SST shown in Figure 1a. On the other hand, through the distribution of SSVD, energy generation and energy flux along the coastal shelf zone (Figures 4a, 6a and 6e) and along the cross-shore section (Figures 8a-c), it becomes evident that the generation and propagation of ITs on the shelf show strong spatial variability.

At the Angolan shelf, the eastern boundary upwelling system is largely influenced by coastally trapped waves that have a semi-annual period [*Rouault*, 2012] and contribute to the seasonal variations in stratification [*Tchipalanga et al.*, 2018]. However, as mentioned above, the high productivity during austral winter cannot be supported only by upwelling due to alongshore winds, which are in their weakest phase in that period. Here, we have explored the possibility that seasonal stratification variations impact IT activity representing a mechanism that supports seasonal variability in near-coastal SST anomalies and primary productivity. The total energy generation at the main generation site (at depths between 100 and 500 m, see Figure 9a) differs only slightly between July and March, which suggests the seasonal variability of energy generation is weak. The energy dissipation shows seasonal variability with high spatial variability in the alongshore (Figures 6g and 6h) and cross-shore directions (Figure 9b). The onshore energy flux also shows different seasonal variability in different regions along the shelf (Figures 6e and 6f). For instance, weaker stratification in July favors enhanced onshore energy flux for section C1 and C3 while it was found the other way around for section C2 (Figures 8a - 8c). Overall, the spatially averaged onshore energy flux is only slightly enhanced in austral winter representing a period of weaker stratification (Figure 8d). *Hall et al.* [2013], based on 2D continental slope/shelf simulations, found that stronger stratification on the shelf favors onshore IT energy flux while for weaker stratification the energy flux is substantially reduced. But the situation differs from here. In their weak stratification case the pycnocline is at the depth of the critical slope at around 600-m depth with very weak or no stratification on the shelf. On the Angolan shelf, the pycnocline is always shallower than 100 m and main IT activity occurs shallower than 200 m. In fact, the near-surface stratification on the Angolan shelf is always strong enough to be favorable to M2 tidal energy transmission even in austral winter with relatively weak stratification (Figure 2d). However, in terms of the IT energy budget, our results show only a weak seasonality in IT energy generation at the continental slope, energy flux onto the shelf and finally dissipation near the coast. This suggests that the seasonality of the IT characteristics do not play a major role in the seasonality of near-coastal surface cooling and upward nutrient supply into the euphotic zone. Nevertheless, some IT characteristics show substantial seasonal variability: the SSVD shows stronger signals along the shelf in July compared to March (Figure 6a) which is generally consistent with the observations of *Ostrowski et al.* [2009] that ITs/internal waves are more coherent and larger in amplitude in austral winter compared to in austral summer.

To quantify mixing by ITs, we suggest an index that is based on the resulting stratification changes. Here we define a parameter *R*, the relative change of the vertical density gradient with respect to the initial gradient:

$$R = \left(\frac{\partial \overline{\rho(z)}}{\partial z} - \frac{\partial \rho_{ini}(z)}{\partial z} \right) \Bigg/ \frac{\partial \rho_{ini}(z)}{\partial z} \times 100\% , \qquad (9)$$

where $\overline{\rho(z)}$ is the averaged density over the last 2 M2 tidal cycles and $\rho_{ini}(z)$ the initial density. Figures 10a and 10b show *R* along section C1 for July and March. The strongest changes in the vertical density gradient are found in the near-surface layers. The maximum absolute values (- 61.21% in July and - 57.53% in March) appear very close to the shore. Mixing is stronger in July as a whole, especially in regions shallower than 50 m. In addition we note that several large values of *R* appear near the bottom at around 13.45°E. This may indicate the interaction of ITs with bottom topography.

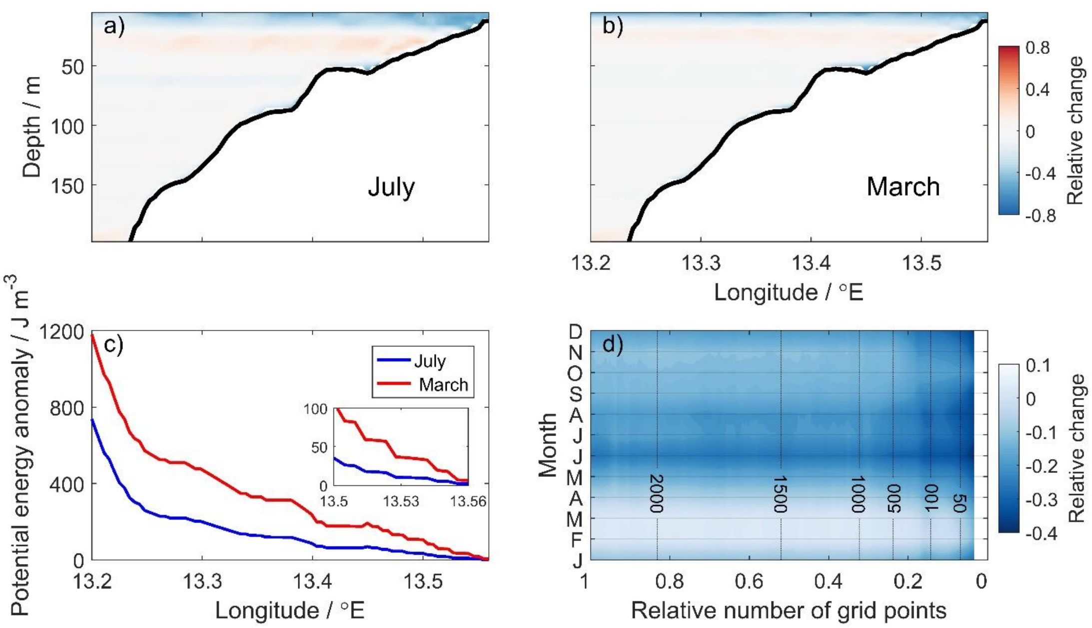

Figure 10. The relative change of the vertical density gradient R along section C1 for a) July and b) March. c) Averaged potential energy anomaly along section C1. d) Seasonal spatially-averaged relative change of near-surface (upper 20 m) vertical density gradient nsR; black dashed lines with numbers are isobaths (unit: m).

Next, we use the potential energy anomaly [*Simpson*, 1981; *Burchard & Hofmeister*, 2008] to evaluate the amount of mechanical energy per unit volume required to instantaneously homogenize the water column. For each water column, the potential energy anomaly is:

$$\phi = \frac{1}{H+\eta}\int_{-H}^{\eta}\left[\overline{\rho_v} - \rho(z)\right] gz\,dz\,, \qquad (10)$$

where $\rho(z)$ is the density, g the gravitational acceleration. The vertical-averaged density $\overline{\rho_v}$ is:

$$\overline{\rho_v} = \frac{1}{H+\eta}\int_{-H}^{\eta}\rho(z)\,dz\,. \qquad (11)$$

The potential energy anomalies along section C1 for July and March computed from observations are shown in Figure 10c. In March, more energy is needed to homogenize the initial stratification along section C1. As the domain averaged generation of IT energy and its onshore propagation has weak seasonal variation, the amount of IT energy on the shelf available for mixing is similar throughout the year. The stratification along the Angolan continental slope/shelf, however, shows a substantial seasonal variability (Figure 2), which represents a preconditioning for the mixing on the shelf. Note that the observed seasonal stratification used in the simulations is modulated by tidal mixing. However, this effect should be small as the observed data used to derive the climatology are from hydrographic profiles taken at water depths between 200 and 800 m [*Kopte et al.*, 2017] while the strongest tidal mixing is simulated at water depths shallower than 50 m. The main conclusion from our study is that with about the same amount of IT energy available on the shelf throughout the year, the water column can be much more effectively mixed during months with a weak stratification, e.g., during July, compared to months with a strong stratification, e.g., during March (Figure 10b). The strongest mixing occurs thereby always close to the coast in water depth shallower than 50 m resulting in a small stripe along the coast with colder SST anomalies most pronounced during austral winter.

We also calculate the near-surface *R* [referred to as *nsR*] which is *R* averaged over the upper 20 m of the water column. Figure 10d shows the seasonal variation of spatially averaged *nsR*. Mixing on the shelf is stronger during austral winter, which is mainly the result of weaker stratification. Compared to the spatial change, the temporal variation is much larger, especially in regions shallower than 500 m. This provides evidence for the seasonality of mixing due to ITs on the shelf and gives some insight into the seasonality of water mass properties and primary productivity along the Angolan coast [*Ostrowski et al.*, 2009].

Similarly to the Angolan upwelling, the tropical upwelling system off the coast of Peru shows a seasonal productivity maximum together with a cross-shore temperature gradient during austral winter when the alongshore winds reach seasonal minimum [*Echevin et al.*, 2008]. Also in this region IT could contribute to near coastal cooling and upward nutrient flux. Our work provides a preliminary framework for understanding the 3D generation and propagation of ITs and their seasonal variations on the Angolan shelf. Yet there are still some additional processes that need to be addressed in later work. For example, our model resolution is not high enough to allow nonhydrostatic short internal waves to develop. These nonlinear ISWs, which are suggested to vary seasonally along the Angolan shelf [*Ostrowski et al.*, 2009], are missing in our simulations. They develop from the disintegration of ITs [*Lamb et al.*, 2004; *Apel*, 2003] and may affect surface cooling and nutrient supply to the euphotic zone by the formation of wave-driven overturning circulations or by the elevated velocity shear and wave breaking [*Zhang et al.*, 2015]. Resolving ISWs would likely not significantly impact the total dissipation of IT energy on the shelf [*Lamb*, 2014], but it could affect the distribution of the dissipation both horizontally and vertically. However, ISW simulations would require a horizontal resolution of few meters, which cannot be achieved in the current 3D model framework, and 2D simulations are likely a better option to address the potential role of ISWs in the biological productivity on the Angolan shelf.

Acknowledgments

This work is supported by the project ‘‘Oceanic Instruments Standardization Sea Trials (OISST)’’ of National Key Research and Development Plan (2016YFC1401300), the Taishan Scholars Program and the China Scholarship Council. The moored ADCP data were acquired within the SACUS project (03G0837A) supported by the German Federal Ministry of Education and Research and further funding was received from the BANINO project (03F0795A) by the German Federal Ministry of Education and Research, from the EU FP7/2007-2013 under grant agreement 603521 PREFACE project and from the EU H2020 under grant agreement 817578 TRIATLAS project. Temperature and salinity data were acquired within the monitoring component of the Nansen Program, in cooperation with the Instituto Nacional de Investigacao Pesqueira (INIP) in Angola and funded by the Norwegian Agency for Development Cooperation (Norad). The SAR image was acquired by the ERS-1 satellite and is downloaded from https://earth.esa.int/web/guest/missions/esa-operational-eo-missions/ers/instruments/sar/applications/tropical/-/asset_publisher/tZ7pAG6SCnM8/content/upwelling-angola. The MODIS SST data is

downloaded from https://podaac-opendap.jpl.nasa.gov/opendap/allData/modis/L3/aqua/11um/v2014.0/4km/8day/2013/contents.html.

References

Alford, M. H., Peacock, T., MacKinnon, J. A., Nash, J. D., Buijsman, M. C., Centurioni, L. R., et al. (2015). The formation and fate of internal waves in the South China Sea. *Nature*, 521(7550), 65-69. https://doi.org/10.1038/nature14399

Apel, J. R. (2003). A new analytical model for internal solitons in the ocean. *Journal of Physical Oceanography*, 33(11), 2247-2269. https://doi.org/10.1175/1520-0485(2003)033<2247:ANAMFI>2.0.CO;2

Bachelery, M. L., Illig, S., & Dadou, I. (2016). Interannual variability in the South-East Atlantic Ocean, focusing on the Benguela Upwelling System: Remote versus local forcing. *Journal of Geophysical Research: Oceans*, 121(1), 284-310. https://doi.org/284-310, 10.1002/2015jc011168

Brandt, P., Rubino, A., Alpers, W., & Backhaus, J. O. (1997). Internal waves in the Strait of Messina studied by a numerical model and synthetic aperture radar images from the ERS 1/2 satellites. *Journal of Physical Oceanography*, 27(5), 648-663. https://doi.org/10.1175/1520-0485(1997)027<0648:IWITSO>2.0.CO;2

Buijsman, M. C., Legg, S., & Klymak, J. (2012). Double-ridge internal tide interference and its effect on dissipation in Luzon Strait. *Journal of Physical Oceanography*, 42(8), 1337-1356. https://doi.org/10.1175/JPO-D-11-0210.1

Buijsman, M. C., Klymak, J. M., Legg, S., Alford, M. H., Farmer, D., MacKinnon, J. A., et al. (2014). Three-dimensional double-ridge internal tide resonance in Luzon Strait. *Journal of Physical Oceanography*, 44(3), 850-869. https://doi.org/10.1175/JPO-D-13-024.1

Burchard, H., & Hofmeister, R. (2008). A dynamic equation for the potential energy anomaly for analysing mixing and stratification in estuaries and coastal seas. *Estuarine, coastal and shelf science*, 77(4), 679-687. https://doi.org/10.1016/j.ecss.2007.10.025

Cacchione, D., & Wunsch, C. (1974). Experimental study of internal waves over a slope. *Journal of Fluid Mechanics*, 66(2), 223-239. https://doi.org/10.1017/S0022112074000164

Carr, M. E., & Kearns, E. J. (2003). Production regimes in four Eastern Boundary Current systems. *Deep Sea Research Part II: Topical Studies in Oceanography*, 50(22-26), 3199-3221. https://doi.org/10.1016/j.dsr2.2003.07.015

Dauxois, T., Didier, A., & Falcon, E. (2004). Observation of near-critical reflection of internal waves in a stably stratified fluid. *Physics of Fluids*, 16(6), 1936-1941. https://doi.org/10.1063/1.1711814

Davidson, F. J., Greatbatch, R. J., & Goulding, A. D. (1998). On the net cyclonic circulation in large stratified lakes. *Journal of physical oceanography*, 28(3), 527-534. https://doi.org/10.1175/1520-0485(1998)028<0527:OTNCCI>2.0.CO;2

Dorostkar, A., Boegman, L., & Pollard, A. (2017). Three-dimensional simulation of high-frequency nonlinear internal wave dynamics in Cayuga Lake. *Journal of Geophysical Research: Oceans*, 122(3), 2183-2204. https://doi.org/10.1002/2016JC011862

Echevin, V., Aumont, O., Ledesma, J., & Flores, G. (2008). The seasonal cycle of surface chlorophyll in the Peruvian upwelling system: A modelling study. *Progress in Oceanography*, 79(2-4), 167-176. https://doi.org/10.1016/j.pocean.2008.10.026

Egbert, G. D., & Erofeeva, S. Y. (2002). Efficient inverse modeling of barotropic ocean tides. *Journal of Atmospheric and Oceanic Technology*, 19(2), 183-204. https://doi.org/10.1175/1520-0426(2002)019<0183:EIMOBO>2.0.CO;2

Gilbert, D., & Garrett, C. (1989). Implications for ocean mixing of internal wave scattering off irregular topography. *Journal of physical oceanography*, 19(11), 1716-1729. https://doi.org/10.1175/1520-0485(1989)019<1716:IFOMOI>2.0.CO;2

Guo, C. C., & Chen, X. (2012). Numerical investigation of large amplitude second mode internal solitary waves over a slope-shelf topography. *Ocean Modelling*, 42, 80-91. https://doi.org/10.1016/j.ocemod.2011.11.003

Hall, R. A., Huthnance, J. M., & Williams, R. G. (2013). Internal wave reflection on shelf slopes with depth-varying stratification. *Journal of physical oceanography*, 43(2), 248-258. https://doi.org/10.1175/JPO-D-11-0192.1

Han, B., & Eden, C. (2019). The energetics of internal tides at the Luzon Ridge. *Ocean Dynamics*, 69(9), 1009-1022. https://doi.org/10.1007/s10236-019-01297-9

Helfrich, K. R., & Grimshaw, R. H. (2008). Nonlinear disintegration of the internal tide. *Journal of Physical Oceanography*, 38(3), 686-701. https://doi.org/10.1175/2007JPO3826.1

Johnston, T. S., & Merrifield, M. A. (2003). Internal tide scattering at seamounts, ridges, and islands. *Journal of Geophysical Research: Oceans*, 108(C6), 3180. https://doi.org/10.1029/2002JC001528

Kelly, S. M., & Nash, J. D. (2010). Internal-tide generation and destruction by shoaling internal tides. *Geophysical Research Letters*, 37(23), L23611. https://doi.org/10.1029/2010GL045598

Klymak, J. M., & Legg, S. M. (2010). A simple mixing scheme for models that resolve breaking internal waves. *Ocean Modelling*, 33(3-4), 224-234. https://doi.org/10.1016/j.ocemod.2010.02.005

Kopte, R., Brandt, P., Dengler, M., Tchipalanga, P. C. M., Macuéria, M., & Ostrowski, M. (2017). The Angola Current: Flow and hydrographic characteristics as observed at 11°S. *Journal of Geophysical Research: Oceans*, 122(2), 1177-1189. https://doi.org/10.1002/2016JC012374

Lamb, K. G. (2004). Nonlinear interaction among internal wave beams generated by tidal flow over supercritical topography. *Geophysical Research Letters*, 31(9), L09313. https://doi.org/10.1029/2003GL019393

Lamb, K. G. (2014). Internal wave breaking and dissipation mechanisms on the continental slope/shelf. *Annual Review of Fluid Mechanics*, 46, 231-254. https://doi.org/10.1146/annurev-fluid-011212-140701

Large, W. G., McWilliams, J. C., & Doney, S. C. (1994). Oceanic vertical mixing: A review and a model with a nonlocal boundary layer parameterization. *Reviews of Geophysics*, 32(4), 363-403. https://doi.org/10.1029/94RG01872

Legg, S., & Adcroft, A. (2003). Internal wave breaking at concave and convex continental slopes. *Journal of Physical Oceanography*, 33(11), 2224-2246. https://doi.org/10.1175/1520-0485(2003)033<2224:IWBACA>2.0.CO;2

Legg, S. (2014). Scattering of low-mode internal waves at finite isolated topography. *Journal of physical oceanography*, 44(1), 359-383. https://doi.org/10.1175/JPO-D-12-0241.1

Leith, C. E. (1996). Stochastic models of chaotic systems. *Physica D: Nonlinear Phenomena*, 98(2-4), 481-491. https://doi.org/10.1016/0167-2789(96)00107-8

MacKinnon, J. A., Zhao, Z., Whalen, C. B., Waterhouse, A. F., Trossman, D. S., Sun, O. M., et al. (2017). Climate process team on internal wave–driven ocean mixing. *Bulletin of the American Meteorological Society*, 98(11), 2429-2454. https://doi.org/10.1175/BAMS-D-16-0030.1

Mathur, M., Carter, G. S., & Peacock, T. (2014). Topographic scattering of the low-mode internal tide in the deep ocean. *Journal of Geophysical Research: Oceans*, 119(4), 2165-2182. https://doi.org/10.1002/2013JC009152

Marshall, J., Hill, C., Perelman, L., & Adcroft, A. (1997). Hydrostatic, quasi-hydrostatic, and nonhydrostatic ocean modeling. *Journal of Geophysical Research: Oceans*, 102(C3), 5733-5752. https://doi.org/10.1029/96JC02776

Mohanty, S., Rao, A. D., & Pradhan, H. K. (2017). Estimates of internal tide energetics in the western Bay of Bengal. *IEEE Journal of Oceanic Engineering*, 43(4), 1015-1023. https://doi.org/10.1109/JOE.2017.2765978

Mohrholz, V., Schmidt, M., & Lutjeharms, J. R. E. (2001). The hydrography and dynamics of the Angola-Benguela Frontal Zone and environment in April 1999: BENEFIT Marine Science. *South African Journal of Science*, 97(5-6), 199-208. https://hdl.handle.net/10520/EJC97324

Mohrholz, V., Bartholomae, C. H., Van der Plas, A. K., & Lass, H. U. (2008). The seasonal variability of the northern Benguela undercurrent and its relation to the oxygen budget on the shelf. *Continental Shelf Research*, 28(3), 424-441. https://doi.org/10.1016/j.csr.2007.10.001

Mohrholz, V., Eggert, A., Junker, T., Nausch, G., Ohde, T., & Schmidt, M. (2014). Cross shelf hydrographic and hydrochemical conditions and their short term variability at the northern Benguela during a normal upwelling season. *Journal of Marine Systems*, 140, 92-110. https://doi.org/10.1016/j.jmarsys.2014.04.019

Munk, W., & Wunsch, C. (1998). Abyssal recipes II: Energetics of tidal and wind mixing. *Deep-sea research Part I: Oceanographic research papers*, 45(12), 1977-2010. https://doi.org/10.1016/S0967-0637(98)00070-3

Nash, J. D., Kunze, E., Toole, J. M., & Schmitt, R. W. (2004). Internal tide reflection and turbulent mixing on the continental slope. *Journal of Physical Oceanography*, 34(5), 1117-1134. https://doi.org/10.1175/1520-0485(2004)034<1117:ITRATM>2.0.CO;2

Nash, J. D., Alford, M. H., & Kunze, E. (2005). Estimating internal wave energy fluxes in the ocean. *Journal of Atmospheric and Oceanic Technology*, 22(10), 1551-1570. https://doi.org/10.1175/JTECH1784.1

Niwa, Y., & Hibiya, T. (2004). Three-dimensional numerical simulation of M2 internal tides in the East China Sea. *Journal of Geophysical Research: Oceans*, 109(C4), C04027. https://doi.org/10.1029/2003JC001923

Ostrowski, M., Da Silva, J. C., & Bazik-Sangolay, B. (2009). The response of sound scatterers to El Niño-and La Niña-like oceanographic regimes in the southeastern Atlantic. *ICES Journal of Marine Science*, 66(6), 1063-1072. https://doi.org/10.1093/icesjms/fsp102

Rouault, M. (2012). Bi-annual intrusion of tropical water in the northern Benguela upwelling. *Geophysical Research Letters*, 39(12), L12606. https://doi.org/10.1029/2012GL052099

Schmidtko, S., Johnson, G. C., & Lyman, J. M. (2013). MIMOC: A global monthly isopycnal upper-ocean climatology with mixed layers. *Journal of Geophysical Research: Oceans*, 118(4), 1658-1672. https://doi.org/10.1002/jgrc.20122

Shaw, P. T., Ko, D. S., & Chao, S. Y. (2009). Internal solitary waves induced by flow over a ridge: With applications to the northern South China Sea. *Journal of Geophysical Research: Oceans*, 114(C2), C02019. https://doi.org/10.1029/2008JC005007

Simpson, J. H. (1981). The shelf-sea fronts: implications of their existence and behaviour. *Philosophical Transactions of the Royal Society of Londo: Series A, Mathematical and Physical Sciences*, 302(1472), 531-546. https://doi.org/10.1098/rsta.1981.0181

Tchipalanga, P., Dengler, M., Brandt, P., Kopte, R., Macuéria, M., Coelho, P., et al. (2018). Eastern boundary circulation and hydrography off angola: building angolan oceanographic capacities. *Bulletin of the American Meteorological Society*, 99(8), 1589-1605. https://doi.org/10.1175/BAMS-D-17-0197.1

Vlasenko, V., Stashchuk, N., Inall, M. E., & Hopkins, J. E. (2014). Tidal energy conversion in a global hot spot: On the 3-D dynamics of baroclinic tides at the Celtic Sea shelf break. *Journal of Geophysical Research: Oceans*, 119(6), 3249-3265. https://doi.org/10.1002/2013JC009708

Venayagamoorthy, S. K., & Fringer, O. B. (2006). Numerical simulations of the interaction of internal waves with a shelf break. *Physics of Fluids*, 18(7), 076603. https://doi.org/10.1063/1.2221863

Zhang, Z., Fringer, O. B., & Ramp, S. R. (2011). Three-dimensional, nonhydrostatic numerical simulation of nonlinear internal wave generation and propagation in the South China Sea. *Journal of Geophysical Research: Oceans*, 116(C5), C05022. https://doi.org/10.1029/2010JC006424

Zhang, S., Alford, M. H., & Mickett, J. B. (2015). Characteristics, generation and mass transport of nonlinear internal waves on the Washington continental shelf. *Journal of Geophysical Research: Oceans*, 120(2), 741-758. https://doi.org/10.1002/2014JC010393